

Characterization of Tensile Properties, Limiting Strains, and Deep Drawing Behavior of AA5754-H22 Sheet at Elevated Temperature

Sudhy S. Panicker, Har Govind Singh, Sushanta Kumar Panda, and Richard Dashwood

(Submitted July 9, 2015; in revised form August 24, 2015; published online October 26, 2015)

Automotive industries are very much interested in characterization of formability improvement of aluminum alloys at elevated temperatures before designing tools, heating systems, and processing sequences for fabrication of auto-body panels by warm forming technology. In this study, tensile tests of AA5754-H22 aluminum alloy were carried out at five different temperatures and three different strain rates to investigate the deformation behavior correlating with Cowper-Symonds constitutive equation. Laboratory scale warm forming facilities were designed and fabricated to perform limiting dome height and deep drawing tests to evaluate forming limit strains and drawability of sheet metal at different tool temperatures. The forming limit strain and dome height improved significantly when both the die and punch were heated to 200 °C. Remarkable improvement in deep drawn cup depth was observed when die and punch temperatures were maintained at 200 and 30 °C, respectively, producing a non-isothermal temperature gradient of approximately 93 °C across the blank from flange to center. The forming behavior at different isothermal and non-isothermal conditions were predicted successfully using a thermo-mechanical FE model incorporating temperature-dependent properties in Barlat-89 yield criterion coupled with Cowper-Symonds hardening model, and the thinning/failure location in deformed cups were validated implementing the experimental limiting strains as damage model.

Keywords AA5754-H22, deep drawing, FE simulation, limiting dome height, warm forming

1. Introduction

The low carbon steel was prevalent in the manufacturing of automotive body components because of their cost effectiveness and good formability at room temperature. The necessitation of improved safety, fuel efficiency, and better properties of formed parts compelled automotive manufacturers to produce lightweight components without compromising the design and strength. Therefore, the material selection scenario is changing to include lighter materials such as aluminum, magnesium, and titanium alloys, and metal matrix and polymer composites. Among different commercially available aluminum alloys, the strain hardenable AA5754 is extensively used in automotive industry because of its high strength to weight ratio, excellent corrosion resistance even in saline atmosphere, and very high toughness even at temperature near to absolute zero (Ref 1). The major hindrance in using aluminum alloys to fabricate critical auto-body components is their inferior formability at room temperature when compared to low carbon steels. Different techniques such as electromagnetic forming (Ref 2),

hydroforming (Ref 3), warm forming (Ref 4), warm hydroforming (Ref 5), and gas forming (Ref 6) are being introduced to enhance their formability. The warm forming technique is a promising and oldest technique, in which the modification of an existing tooling is not as complicated when compared to other methods. The use of AA5754 sheets are sometimes limited to inner body panels because of poor surface finish due to undesirable stretch markings on the surface when formed at room temperature. This is because of Portvein-Le Chatelier (PLC) effect which is a macroscopic indication of dynamic strain aging, and this is clearly visible as a serration flow in the uniaxial tensile testing results (Ref 7). It has been demonstrated by Bolt et al. (Ref 8) that this defect disappears when the component is deformed at warm conditions. The uniaxial tensile test performed by Ozturk et al. (Ref 9) on AA5754 showed an increase in total elongation without serration at cryogenic temperatures and warm conditions. The strain rate hardening effect causes its increase in formability at warm conditions while increased elongation at cryogenic temperature is associated with work-hardening phenomena. The critical role of strain rate sensitivity on warm formability of three aluminum alloys-AA5182, AA5754, and AA6111-T4 was investigated by Li and Ghosh (Ref 10). The uniaxial tensile tests were performed in the temperature range of 200-350 °C with varying strain rates of 0.015-1.5 s⁻¹, and it was observed that slow strain rate at elevated temperature provided a substantial improvement in post-uniform elongation and true fracture strain. It was also reported that the warm formability of 5xxx series alloys was superior to precipitation hardened 6xxx series alloys. Jain et al. (Ref 11) reported that reduction in die profile radius resulted in decreased limiting drawing ratio (LDR) and increased the tendency of ironing and subsequent fracture. The effect of blank holding force (BHF) on warm deep drawing of

Sudhy S. Panicker, Har Govind Singh, and Sushanta Kumar Panda, Department of Mechanical Engineering, Indian Institute of Technology, Kharagpur, Kharagpur 721302, India; and **Richard Dashwood**, Warwick Manufacturing Group, University of Warwick, Coventry CV4 7AL, UK. Contact e-mail: sushanta.panda@mech.iitkgp.ernet.in.

magnesium alloy at elevated temperature was studied by Yoshihara et al. (Ref 12). The localized cooling at blank center region was developed, and a drastic improvement in LDR emphasizing the need of proper temperature distribution across the blank was proposed. The deep drawing experiments on AA5754-O aluminum alloy sheet by Palumbo and Tricarico (Ref 13) showed that temperature gradient on the blank has a significant effect on LDR for warm deep drawing. The experimental results were compared by performing FE analysis in ABAQUS with a fully thermo-coupled model. The influence of punch speed on the formability was also emphasized. FE validation of deep drawn rectangular cup for AA5182 sheet at warm conditions was performed by Kim et al. (Ref 14). The effect of temperature gradient on the failure location was studied by measuring the strain distribution and thickness distribution. Sheet metal forming essentially undergoes biaxial deformation rather than tensile elongation (Ref 15). Therefore, Li and Ghosh (Ref 16) studied the biaxial deformation behavior of AA5182, AA5754, and AA6111-T4 alloys and reported that forming limit diagram (FLD) evaluated at 250 °C for automotive aluminum alloy sheet were comparable to low carbon aluminum killed steel at room temperature. They achieved higher part depth without much loss in post-forming yield strength by keeping the punch temperature 50 °C lesser than that of die. Naka et al. (Ref 17) performed stretch forming operation for fine-grained AA5083 alloy sheet at temperature range of 20-300 °C with varying deformation rate of 0.2-200 mm/min. A significant rise in limiting strain level was noticed at 300 °C condition with lowest deformation rate of 0.2 mm/min.

The formability prediction and faster optimisation of sheet metal forming process is possible through finite element modeling with proper selection of process parameters. Selection of an appropriate hardening rule and yield criterion are crucial in FE simulation of aluminum alloy sheet as discussed elsewhere (Ref 18-22). In 1989, Barlat and Lian (Ref 18) proposed a yield criterion that describes the behavior of orthotropic sheet metals exhibiting planar anisotropy and subjected to plane stress condition. The influence of yield criteria on formability prediction of Al-5% Mg alloy was described by Yoon et al. (Ref 19). The true stress-true strain data obtained from bulge test were curve fitted to Voce hardening rule for prediction of formability. The finite element modeling of stamp hydroforming process simulations using Barlat-89 model predicted accurate results when compared with experimental results done by Zampaloni et al. (Ref 20). The variation of yield locus with temperature for AA5083-O aluminum alloy was experimentally determined by Naka et al. (Ref 21).

There were no open literature available on analyzing the influence of temperature in the formability of AA5754-H22 aluminum alloy imposing non-isothermal conditions. AA5754 aluminum alloy in H22 temper condition was chosen because of its relative high strength and ductility when compared to other tempered form. Therefore, in this research, an attempt has been made to get an insight into the warm temperature formability of the material by conducting a series of laboratory scale tensile testing, stretch forming, and deep drawing experiments. Stretch forming experiments comprised the evaluation of limiting dome height (LDH) at room temperature and isothermal elevated temperature at 200 °C. Deep drawing tests were conducted at both isothermal and non-isothermal conditions by heating the die and punch independently. Fully

coupled thermo-mechanical FE simulation of both stretch forming and deep drawing processes were also performed. The predicted LDHs, strain distribution, deep drawing cup depth, thinning development, and earing profile were validated with the experimental data.

2. Materials and Methods

The aluminum alloy—AA5754 in H22 temper condition was selected in the present study. The 1.0-mm-thick sheet metal was obtained from the manufacturer after rolling and subsequent partial annealing, and the chemical composition is presented in Table 1. The presence of Mg and Mn solute atoms in this alloy increases strain hardening due to the stress field developed in the crystal around these atoms, which hinders dislocation propagation and/or multiplication. Recently, the automotive industries are paying attention to enhance the application of this non-heat treatable Al-Mg alloy in manufacturing of light-weight body panels without compromising the crashworthiness.

2.1 Tensile Testing

The tensile properties such as yield strength (*YS*), ultimate tensile strength (*UTS*), and % elongation of AA5754-H22 were evaluated using sub-size specimens as per ASTM E8 standards (Ref 23). The tests were conducted in 0°, 45°, and 90° with respect to rolling direction (*RD*) at five different temperatures 30, 100, 175, 200, and 250 °C, and three different strain rates 0.001, 0.1, and 0.16 s⁻¹. The true stress-true strain responses in the plastic flow regime were correlated with Cowper-Symonds constitutive equation (Eq 1) to describe the influence of strain hardening and strain rate sensitivity.

$$\sigma_y(\dot{\epsilon}_{eff}^p, \dot{\epsilon}_{eff}^p) = \sigma_y^s(\dot{\epsilon}_{eff}^p) \left[1 + \left(\frac{\dot{\epsilon}_{eff}^p}{C} \right)^{\frac{1}{p}} \right], \quad (\text{Eq 1})$$

where σ_y is the yield stress depending on the effective plastic strain $\dot{\epsilon}_{eff}^p$ and effective plastic strain rate $\dot{\epsilon}_{eff}^p$. The terms, *C* and *p* are strain rate sensitivity parameters. The quasi-static yield stress, σ_y^s , is related with plastic strain by following power law relation (Eq 2):

$$\sigma_y^s(\dot{\epsilon}_{eff}^p) = K(\dot{\epsilon}_{eff}^p + \dot{\epsilon}_{eff}^y)^n, \quad (\text{Eq 2})$$

where $\dot{\epsilon}_{eff}^y$ is the initial yield strain and it can be described by Eq 3.

$$\dot{\epsilon}_{eff}^y = \left(\frac{E}{K} \right)^{(1/(n-1))}. \quad (\text{Eq 3})$$

In Eq 3, *E* signifies the Young's modulus. The strain rate sensitivity parameters *C* and *p* and the hardening parameters *K* and *n* were determined at different temperatures after fitting the Eq 1 in the uniaxial true stress-true strain response (between the

Table 1 Chemical composition of as received AA5754-H22 alloy

Element	Mg	Mn	Fe	Si	Al
wt. (%)	2.60-3.20	0.50	0.40	0.40	Balance

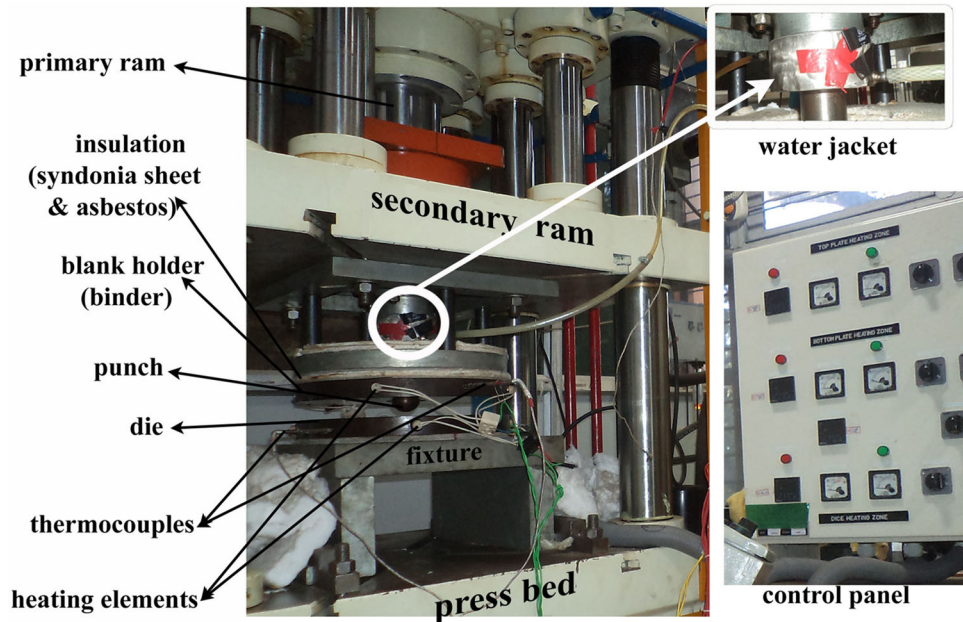


Fig. 1 Double-action hydraulic press with heating arrangements to conduct warm forming experiments

YS and *UTS*). The Lankford anisotropy coefficient or plastic strain ratio (*R* value) of the material was evaluated at different temperatures to assess the variation with temperature. The specimens were elongated to 80% of longitudinal strain corresponding to *UTS* for determining the *R* values (Ref 24). The final width and length of the deformed specimens were measured and *R* values were computed by the following equation:

$$R = \frac{\epsilon_w}{\epsilon_t} = \frac{\epsilon_w}{-(\epsilon_w + \epsilon_l)} = \frac{\ln(w_f/w_0)}{\ln(l_0 w_0 / l_f w_f)}, \quad (\text{Eq 4})$$

where ϵ_w , ϵ_t , and ϵ_l are true strain in width, thickness, and length respectively, w_0 and w_f are initial and final width, l_0 and l_f are initial and final gauge length. The average normal anisotropy of the material was determined using expression $\bar{R} = \frac{1}{4}(R_0 + 2R_{45} + R_{90})$, where R_0 , R_{45} , and R_{90} are the plastic strain ratio along rolling, 45°, and transverse direction of the sheet metal. The 30 °C temperature was referred as room temperature, and the same is followed in the subsequent sections.

2.2 Formability Tests

2.2.1 Warm Forming Test Rig. The stretch forming and deep drawing experiments were performed using a double-acting hydraulic press of 50 ton capacity of both primary and secondary ram. Fig. 1 demonstrates the essential parts of the press where the formability test rig was mounted. Punch was connected to the primary ram, and binder was attached to the pressure pad on secondary ram. The die was fastened on the fixture placed on the press bed. A load cell with linear variable displacement transducer (LVDT) situated at the top of primary ram helped in capturing the load-displacement data throughout the deformation process. In-situ arrangements were provided to heat die, binder, and punch independently through resistance heaters, each of 350 W capacity. The temperatures of tooling were displayed on control panel with the help of thermocouples

embedded in die, binder, and punch, respectively. Thus, a pre-set temperature of the die, binder, and punch were achieved with the aid of cut-off switches in the control panel. Insulation comprising syndonia sheet and glass wool were placed between binder and pressure pad to arrest heat transfer. To obstruct heat transfer to the load cell, the coupler connecting the punch and the primary ram was modified with a water jacket. All the heaters were switched off during room temperature experiments. The process sequences adopted in the present warm forming experiments consisted of five basic steps (a-e) enlisted below:

- The binder was moved down and touched with the die, and the exposed top and side surfaces were covered with the glass wool to diminish convective heat transfer.
- The heaters were switched on to achieve required tooling temperature and the binder was moved up to place and align the blank on the die.
- Adequate blank holding pressure was applied to suppress the wrinkling in the component.
- The punch was moved toward the blank and appropriate dwell time was provided to establish steady temperature in the blank center.
- At last, the blank was deformed by moving the punch at a speed of 20 mm/min and the test was stopped as soon as necking/failure observed through a mirror placed below the die.

All the experiments were planned in dry condition without application of lubrication. Henceforward, the die temperature means temperature of both the die and binder.

2.2.2 Limiting Dome Height Test. The tooling assembly including the punch and dies with heaters for the LDH testing is shown in Fig. 2(a). The circular drawbead was designed at a radius of 36 mm on both the dies to clamp the blank by application of blank holding force. Hence, only the portion of the sheet metal exposed to the die cavity was stretched by the

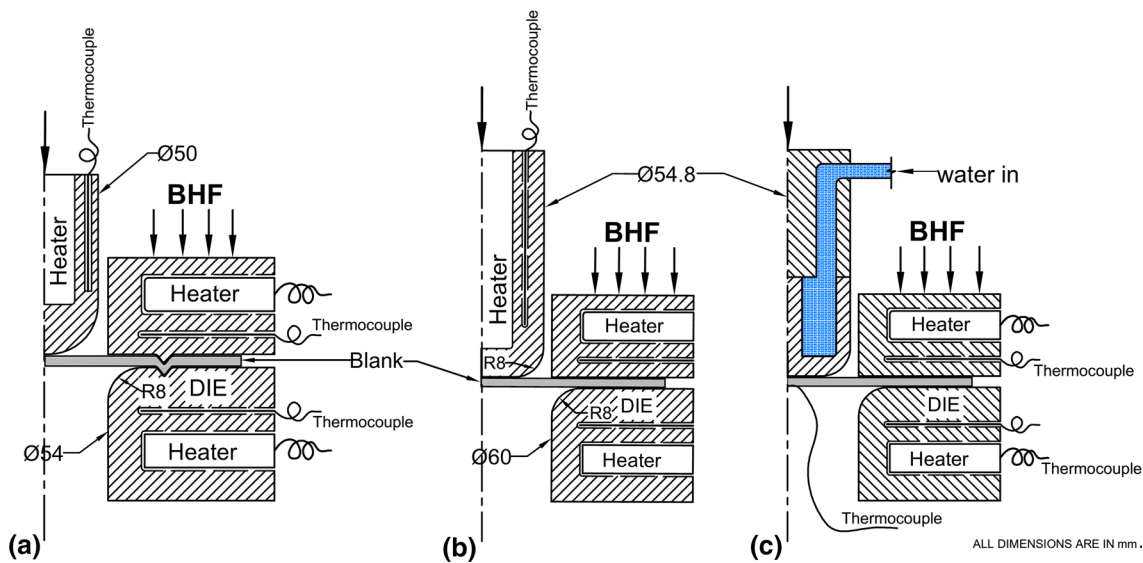


Fig. 2 Schematic of different laboratory scale warm forming test setup developed: (a) stretch forming setup, and deep drawing setup with (b) punch having heater and (c) punch having water cooling provision

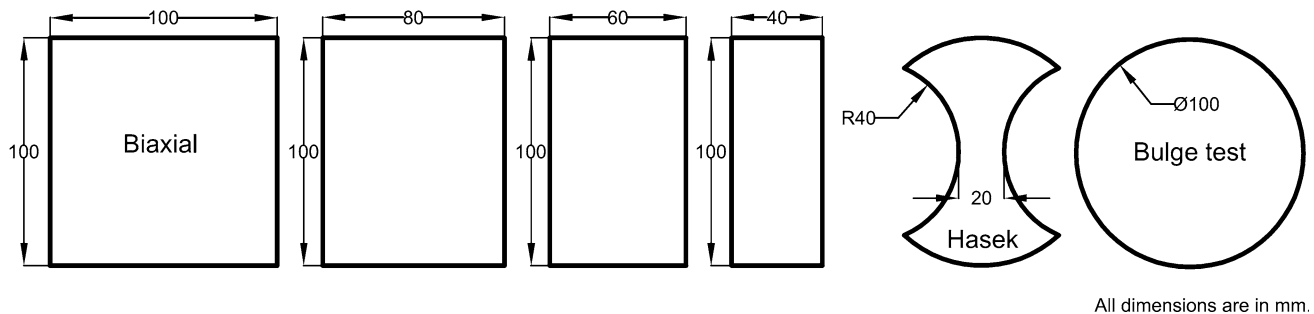


Fig. 3 Different geometry specimen with dimensions for experimental determination of limiting strains to construct forming limit diagram

50-mm-diameter hemispherical punch without drawing of flange materials. The maximum punch displacement at the onset of necking/failure in the blank is identified as the LDH. Several blanks having dimensions as shown in Fig. 3 were used in the test to deform the material in different strain paths. In order to obtain the biaxial strain path, circular blank of 100-mm diameter was fabricated and the bulge test was carried out. The circle grid analysis (CGA) was performed to measure the major and minor strain at different location on the outer surface of the deformed blank. The stretch forming experiments were conducted both at room temperature and elevated temperature (200 °C), but the bulge test at elevated condition was not performed due to the setup limitation. For isothermal (200 °C) LDH test, the blank placed between the dies was held for 10 minutes in order to uniformly heat the blank to the desired temperature.

2.2.3 Deep Drawing Test. The schematic for isothermal deep drawing setup with provisions of inserting electric heater is shown in Fig. 2(b). Another punch with an arrangement of constant water circulation in the punch to conduct non-isothermal deep drawing operation is as shown in Fig. 2(c). The water-circulated cooler punch helped in maintaining a temperature gradient across the blank during the deformation. The variation in the blank center temperature (BCT) was

monitored by placing a thermocouple. Several experimental trials were carried out to achieve proper blank holding force and blank diameter so that deeper cups could be drawn without wrinkling. After a number of trial experiments, BHF and initial blank diameters were selected as 1.5 kN and 110 mm, respectively. As the material strength alters at elevated temperatures, the applied BHF was scaled accordingly. Further, to investigate the influence of the die and punch temperature on the cup height and thickness distribution, the following four deep drawing experiments were performed: 1st—both the die and punch at room temperature, 2nd—both die and punch at 200 °C, 3rd—punch at 120 °C and die at 200 °C, and 4th—punch at 30 °C and die at 200 °C.

2.3 Finite Element Modeling

The thermo-mechanical simulation of the stretch forming and deep drawing process was executed using the LS-971 version of the explicit dynamic finite element code LS-DYNA3D (Ref 25). The mechanical and thermal parts of the problem are solved independently. The mechanical part of problem is solved using explicit dynamic solution scheme, whereas the thermal part is solved using implicit scheme. The bottleneck in computation time is the explicit mechanical time

step which should be less than the time required for a stress wave to cross the smallest element [Courant criterion (Ref 26)]. FE models of stretch forming and deep drawing processes were developed with the pre-processor Dynaform-5.9.2. Taking advantage of symmetry, only quarter model was made in order to reduce computational time. The symmetry boundary conditions were imposed along the sides of the blank in the XZ and YZ planes. All tooling parts treated as rigid bodies assigning material model *MAT_020 with four-node rigid shell element meshing. This will help in increasing computational efficiency as there will be no requirement of storage allocation for deformation history (Ref 25). The four-node quadrilateral Belytschko-Tsay shell elements were used to mesh the deformable blank of thickness 1 mm (Ref 27) with five through thickness integration points. To suppress hourglassing, i.e., zero stress state during deformation, the default LS-DYNA3D hourglass control technique was implemented. The shell element formulation was done using adaptive remeshing scheme with level-4 refinement for better accuracy in results with less number of elements in the model. In order to further reduce computational expense, time-scaling method was adopted and rate dependent properties were scaled accordingly. The punch velocity during simulation was set 1000 mm/s, and the BHF was calibrated since quarter model had been used. For LDH test model, an analytical drawbead was assigned in the binder at 36 mm radius. The input values of static coefficient of friction at tool blank interfaces for different operating conditions are listed in Table 2. It has been reported that the coefficient of friction between blank and punch reduces with increase in temperature (Ref 28). The surface to surface thermal penalty stiffness-based contact algorithm was used to model the contact between the blank and the tooling. A constant thermal gap conductance of 900 W/mK given for the tool and blank interface (Ref 13). Thermal properties used for blank material (aluminum) and tools (steel) are summarized in Table 3. The punch was initially brought into contact with the blank, and subsequently it was kept touching at this position for five seconds to allow heat transfer. As soon as near to steady state condition was reached, the punch was ramped up to its set velocity to deform the material. This technique was used to match the experimental conditions. The reason for allowing the heat transfer to reach a steady state or near steady state condition was to reduce the variability in the experiments, giving more repeatable results and also making them easier to simulate. In the post-processing stage, the forming limit diagram developed at room temperature and 200 °C were used to predict the initiation of necking/crack.

The deformable blanks were modeled using Barlat-89 yield function which take into account both planar and normal anisotropy of aluminum alloy sheet material, defined and executed in LS-DYNA as material type *MAT_036 (Ref 25).

Table 2 Friction coefficient used in FE simulation

Process	Operating temperature	Coefficient of friction
Stretch forming	Room temperature	0.33
	200 °C	0.23
Deep drawing	Room temperature	0.33
	Non-isothermal (Die=200 °C, Punch=30 °C)	0.23 (at die-blank surface interface); 0.33 (at punch-blank surface interface)
	200 °C	0.23

As the thickness of sheet material is negligible compared to other dimensions, deformation considered to be in plane stress state and hence Barlat-89 yield criterion as proposed by Barlat and Lian (Ref 18) can be described as

$$2\bar{\sigma}^M = a|K_1 + K_2|^M + a|K_1 - K_2|^M + c|2K_2|^M, \quad (\text{Eq 5})$$

where $\bar{\sigma}$ is yield stress and M is the Barlat yield surface exponent, and as aluminum has FCC structure, $M = 8$ was selected. The stress invariants, K_1 and K_2 found out as shown in Eq 6.

$$K_1 = \frac{\sigma_x + l\sigma_y}{2}; \quad K_2 = \left[\left(\frac{\sigma_x - l\sigma_y}{2} \right)^2 + q^2\sigma_{xy}^2 \right]^{1/2}, \quad (\text{Eq 6})$$

where σ_x , σ_y , and σ_{xy} are plane stress components in orthotropic axes. The anisotropy material parameters a , c , l , and q can be related to Lankford's parameters R_0 , R_{45} , and R_{90} as described by Barlat and Lian (Ref 18).

Now, taking into account only normal anisotropy, i.e., assuming $R_0 = R_{45} = R_{90} = \bar{R}$, the Eq 5 reduces to an equation in terms of principal stresses.

$$2\bar{\sigma}^M = \frac{2}{1+\bar{R}}|\sigma_1|^M + \frac{2}{1+\bar{R}}|\sigma_2|^M + \frac{2\bar{R}}{1+\bar{R}}|\sigma_1 - \sigma_2|^M. \quad (\text{Eq 7})$$

If the yield function exponent $M = 2$, then Eq 7 transform to Hill-48 (Ref 29) anisotropic yield criterion considering only normal anisotropy.

$$2\bar{\sigma}^2 = \frac{2}{1+\bar{R}}\sigma_1^2 + \frac{2}{1+\bar{R}}\sigma_2^2 + \frac{2\bar{R}}{1+\bar{R}}(\sigma_1 - \sigma_2)^2. \quad (\text{Eq 8})$$

Deep drawing simulation using Hill-48 yield criterion were also done for comparison purpose.

To incorporate strain rate effect in the simulation, Cowper-Symonds constitutive equation (Eq 1) (Ref 30) was employed in the present FE model. It was found that the Lankford anisotropy coefficients (R_0 , R_{45} , R_{90} , and \bar{R}), hardening parameters (K and n -value), and strain rate sensitive parameters C and p were depending on the temperature. The details are discussed

Table 3 Thermal properties of blank and tooling used in FE model (Ref 31)

Properties	Blank (Aluminum)	Rigid tools (steel)
Heat Capacity (J/kgK)	904	450
Thermal Conductivity (W/mK)	220	70
Density (kg/m ³)	2710	7850

in section 3.1, and these temperature-dependent parameters are correlated with temperature to be coupled with Cowper-Symonds equation and Barlat-89 model.

3. Results and Discussion

3.1 Tensile Properties and Cowper-Symonds Constitutive Equation

Engineering stress-strain response of AA5754-H22 alloy specimens obtained from uniaxial tensile test along the rolling direction at a strain rate of 0.001 s^{-1} under five different temperatures: room temperature ($30 \text{ }^\circ\text{C}$), 100, 175, 200, and

$250 \text{ }^\circ\text{C}$ had been compared as shown in the Fig. 4(a). The serrated flow was observed in the material during slow strain rate (0.001 s^{-1}) testing at lower temperatures (both 30 and $100 \text{ }^\circ\text{C}$). It may be due to temporary hindrance of dislocations at high energy state grain boundaries with the presence of solute Mg-atoms. The presence of solute atoms around the grain boundaries may have created stronger barrier, and load bearing capacity increases temporarily with a sharp drop in load once these barriers are torn away (Ref 31). However, the serrated flow was observed to diminish while uniaxial deformation at higher strain rate and elevated temperature, as shown in Fig. 4(a) and (b). The velocity of mobile dislocations during plastic deformation increases at higher strain rate, and this helps in reducing the waiting time of the dislocations at grain

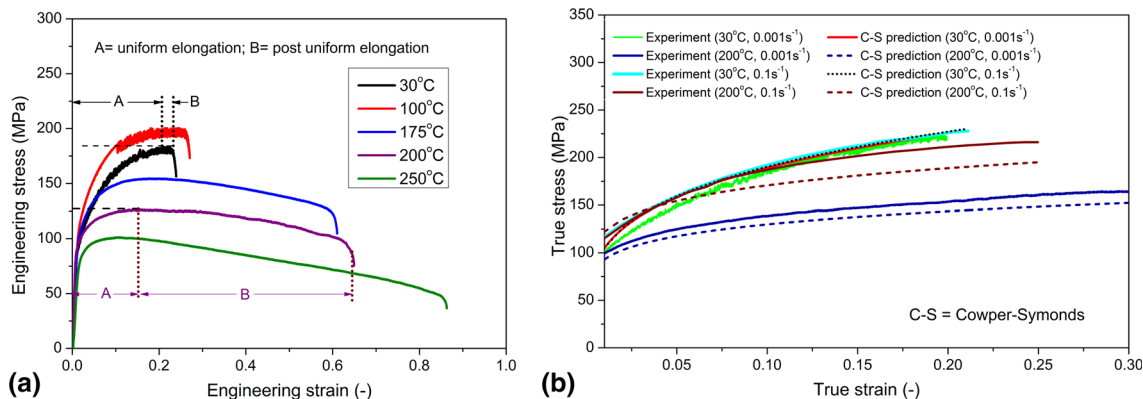


Fig. 4 (a) Effect of temperature on engineering stress-strain response at constant strain rate of 0.001 s^{-1} and (b) Strain rate effect on tensile deformation with validation of Cowper-Symonds constitutive equation

Table 4 Mechanical properties of AA5754-H22 alloys at five different temperatures for a quasi-static strain rate of 0.001 s^{-1}

Temperature, $^\circ\text{C}$	YS, MPa	UTS, MPa	Uniform elongation, %	Post-uniform elongation, %	Total elongation, %
30	87.00	185.00	20.50	4.00	24.5
100	100.00	201.00	24.00	3.70	27.7
175	86.00	155.00	18.50	43.50	62.0
200	82.00	127.00	14.10	49.90	64.0
250	72.50	102.00	11.30	75.20	86.5

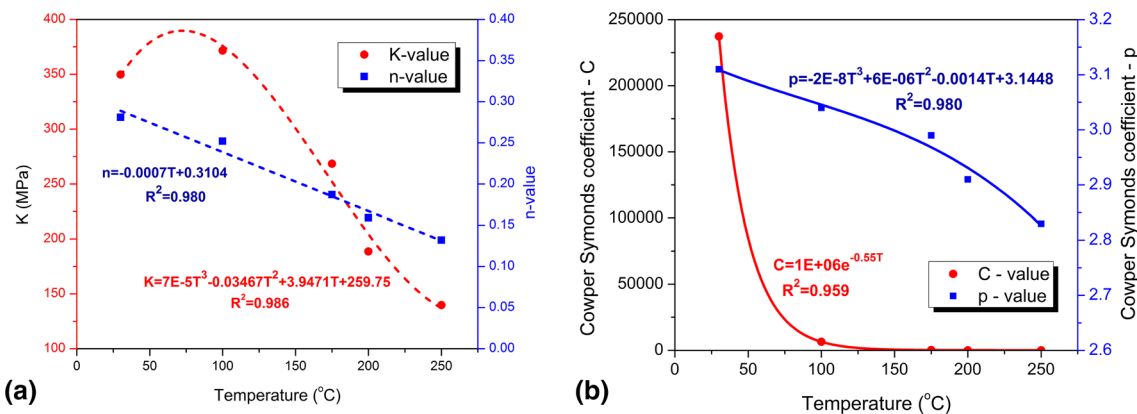


Fig. 5 Variation of Cowper-Symonds parameters with temperature:(a) K and n -value, and (b) C and p value

boundaries. Hence, a weak barrier of solute atoms around the grain boundaries is easily torn away by the movable dislocation (Ref 30). It was noticed that both the YS and UTS increased at $100\text{ }^\circ\text{C}$, and similar results were observed by previous researchers (Ref 7). It was found to be related with the predominance of dynamic strain aging (DSA) under PLC range where temperature has negligible effect on flow stress. The YS and UTS were found to decrease with further increase in temperature, and a sharp reduction was observed at temperatures above $175\text{ }^\circ\text{C}$.

Table 4 summarizes the mechanical properties such as YS , UTS , and total elongations of the sheet metal at quasi-static strain rate of 0.001 s^{-1} . It can be inferred from Table 4 that the reduction in UTS was more sensitive to temperature than YS . The total elongation was observed to increase by 253% with increase in deformation temperature from room temperature to $250\text{ }^\circ\text{C}$, and this reflected the significant improvement in formability of this material. Further, the total elongation was decoupled into uniform and post-uniform elongation as depicted in Fig. 4(a). A gradual decline in uniform elongation from 20.5% to 11.3% was observed when temperature was changed from room temperature to $250\text{ }^\circ\text{C}$. However, significant increase in post-uniform elongation was noticed at elevated temperature beyond $100\text{ }^\circ\text{C}$. The Cowper-Symonds constitutive equation was used to capture the effect of strain rate on the uniaxial deformation behavior of the material. The

variation in Cowper-Symonds material parameters at different temperature was correlated as shown in Fig. 5(a) and (b). It can be seen that the n -value decreased with the increase in deformation temperature, and this is attributed to the reduction in uniform elongation. Similarly, the C and p values were obtained at five different temperatures after non-linear regression of Cowper-Symonds constitutive equation (Eq 1) using true stress and true plastic strain data. The variation of C and p values with temperature is depicted in Fig. 5(b). The higher value of C at room temperature signifies insensitivity of the material at room temperature which can also be seen in Fig. 4(b). The experimental true stress-strain response at room temperature for 0.001 and 0.1 s^{-1} are almost coinciding, while a distinguishable reduction in flow stress is observed for lower strain rate at $200\text{ }^\circ\text{C}$. The significant rise in post-uniform elongation may be due to the strain rate sensitivity of the material at elevated temperature which delayed the onset of strain localization and subsequent failure. Also, both K and n values reduced at elevated temperature (Fig. 5a), and this helped in quantitative decrease in the flow stress resulting reduction in deformation load. The influence of temperature on Lankford anisotropy parameters R_0 , R_{45} , and R_{90} is depicted in Fig. 6, where a polynomial curve fit is used to represent the variations. The increase in these Lankford parameters resulted in 144.1% increase in average normal anisotropy parameter (\bar{R}) at $250\text{ }^\circ\text{C}$ compared to room temperature. This improvement signifies the higher resistance to thinning during sheet forming, which may help in increase in formability of the material at elevated temperature. The R^2 values specified in Fig. 5 and 6 is the coefficient of determination which signifies how well data points fit a curve. The stress-strain responses were plotted at two different temperatures (30 and $200\text{ }^\circ\text{C}$) and strain rates (0.001 and 0.1 s^{-1}) using the modified Cowper-Symonds constitutive equation (Eq 9) incorporating the temperature dependent parameters, and the results were validated with experimental stress-strain response as shown in Fig. 4(b). The equations for the temperature-dependent parameters $K(T)$, $n(T)$, $C(T)$, $p(T)$, $R_0(T)$, $R_{45}(T)$, $R_{90}(T)$, and $\bar{R}(T)$ were obtained after curve fitting the values of respective parameters at different temperatures and are enlisted in Table 5.

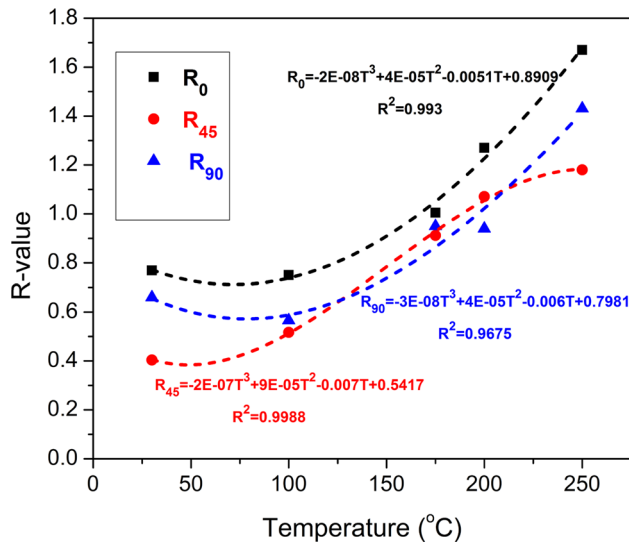


Fig. 6 Variation of Lankford anisotropy parameters with temperature

$$\sigma_y(\epsilon_{eff}^p, \dot{\epsilon}_{eff}^p, T) = K(T) \left(\epsilon_{eff}^p \right)^{n(T)} \left[1 + \left(\frac{\dot{\epsilon}_{eff}^p}{C(T)} \right)^{\frac{1}{p(T)}} \right] \quad (\text{Eq 9})$$

3.2 Forming Limit Diagram

The stretch forming experiments were conducted to evaluate the LDH of varying specimen geometry as discussed in section 2.2.2 at room temperature and elevated temperature

Table 5 Curve-fit equations of temperature-dependent Cowper-Symonds and Lankford anisotropy parameters

Parameters	Curve-fit equation, T in $^\circ\text{C}$	Coefficient of determination, R^2
$K(T)$	$7E-05T^3 - 0.0346T^2 + 3.9471T + 259.75$	0.982
$n(T)$	$0.2791 - 6.869E-4T$	0.991
$C(T)$	$1E + 06e^{-0.55T}$	0.959
$p(T)$	$-2E-8T^3 + 6E-06T^2 - 0.0014T + 3.1448$	0.980
$R_0(T)$	$-2E-8T^3 + 4E-05T^2 - 0.0051T + 0.8909$	0.993
$R_{45}(T)$	$-2E-07T^3 + 9E-05T^2 - 0.0077T + 0.5417$	0.998
$R_{90}(T)$	$-3E-08T^3 + 4E-05T^2 - 0.0067T + 0.7981$	0.968
$\bar{R}(T)$	$-1E-07T^3 + 6E-05T^2 - 0.0063T + 0.6931$	1.000

(200 °C). Fig. 7 shows CGA to evaluate both the major and minor limiting strains from the deformed ellipse lying within a critical region of a 100 × 100 mm specimen deformed at room temperature. It is important to note that the specimens are deformed into the convex shape using the hemispherical punch, and it may have experienced both stretching and bending during the deformation. Previously, researchers (Ref 32) observed that the experimentally determined limit strains were influenced by the bending strains due to the punch curvature. The dependence of tensile bending strain (ϵ_b) induced on the convex surface due to the punch curvature (ρ) can be expressed by bending equation as shown in Eq 10. Hence, the measured surface strains increased with the increase in bending strains leading to a higher forming limit diagram. In order to evaluate the forming limit strains correctly, Eq 12 was used to subtract the bending strain from the measured surface strain ($\epsilon_{m1,2}$). Thus, the effect of punch curvature was corrected for

estimating the true stretching strains for both major and minor strains (ϵ_1 and ϵ_2).

$$\epsilon_b = \ln\left(1 + \frac{t_f}{2\rho}\right), \quad (\text{Eq 10})$$

where t_f is the final thickness and it can be expressed as a function of initial thickness t_0 and measured true major and true minor surface strains as shown in Eq 11.

$$t_f = t_0 \exp(-\epsilon_{m1} - \epsilon_{m2}) \quad (\text{Eq 11})$$

$$\epsilon_{1,2} = \epsilon_{m1,2} - \epsilon_b. \quad (\text{Eq 12})$$

The true major and minor strains at safe, necking, and fracture regions in deformed specimens of different geometries were measured. All these data were plotted in strain space with minor and major strain as abscissa and ordinate, respectively, as shown in Fig. 8. The forming limit diagram (FLD) was constructed to separate the safe zone from the failure zone consisting of necking and fracture strain data. Further, the bending strain correction was incorporated in the entire curve to estimate the corrected FLD. It was observed that the deformed specimens of 100 × 60 mm and 100 × 40 mm dimensions provided data closer to plane strain condition. Even though exact data points were not available for pure plane strain condition, it was considered that the strain value where the FLD intersected the major strain axis as FLD_0 . Mostly, the failure occurred in plane strain condition while stamping an industrial complex components due to lack of lubrication and punch geometry, and further the limiting strains are lowest along plane strain deformation mode. Hence, several researchers considered FLD_0 as a measure of formability, and sheet forming industries are interested in improvement in FLD_0 at elevated temperature apart from the complete FLD as a diagnostic tool. The FLDs evaluated both at room temperature and 200 °C are compared in Fig. 8. All the stretch formed specimens are shown in Fig. 9(a) and (b), and the deformed ellipses on these specimens were measured to generate the limiting strain data for constructing the FLDs as discussed above.

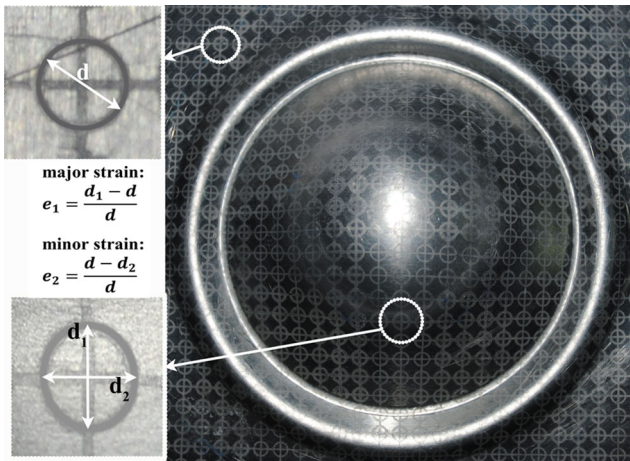


Fig. 7 Circular grid analysis in a stretch formed 100 × 100 mm specimen

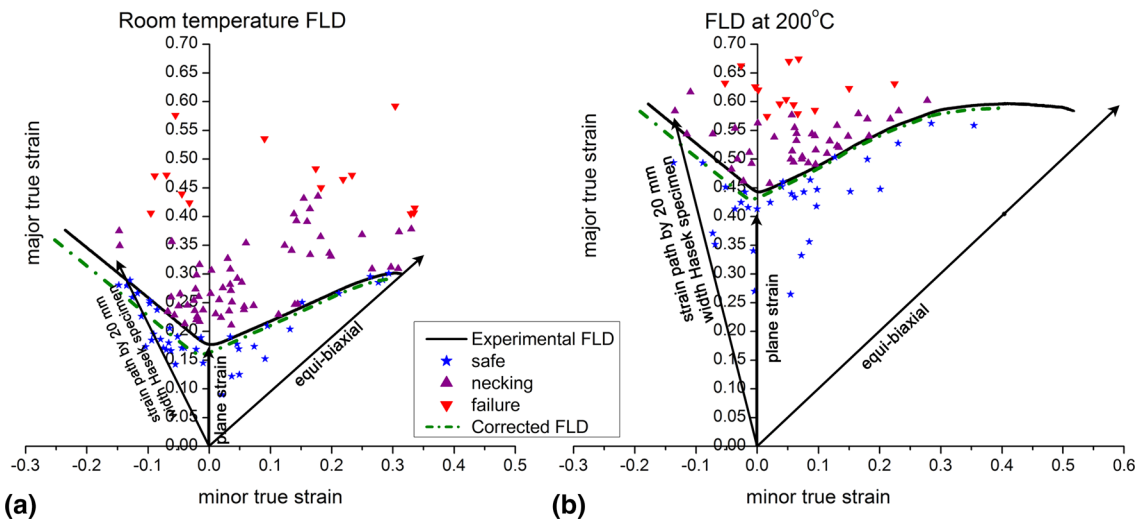


Fig. 8 Forming limit diagrams with bending correction: (a) room temperature and (b) elevated temperature at 200 °C

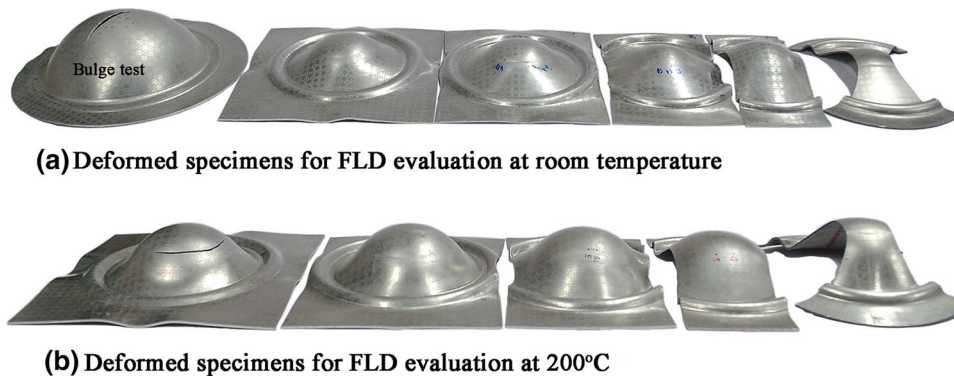


Fig. 9 Deformed LDH test specimens for evaluation of forming limit diagrams: (a) room temperature and (b) elevated temperature at 200 °C

Table 6 Limiting dome height comparison of experimental and FE predicted results at room temperature and 200 °C

Specimen geometry (mm × mm)	Dome height at 30 °C, in mm				Dome height at 200 °C, in mm			
	Expt.	Simulation Results	% error	Expt.	Simulation Results		% error	
					without C&p	with C&p	without C&p	with C&p
100 × 100	14.78 ± 0.08	14.72	0.41	19.06 ± 0.06	14.08	19.01	26.12	0.26
100 × 80	13.86 ± 0.09	13.88	0.14	18.55 ± 0.08	13.89	18.70	25.12	0.81
100 × 60	13.44 ± 0.08	13.00	3.27	16.70 ± 0.07	11.45	17.09	31.44	2.33
100 × 40	16.94 ± 0.07	16.90	0.23	18.48 ± 0.06	13.44	18.75	27.27	1.46
100 × 20 (Hasek)	13.79 ± 0.08	13.80	0.08	17.49 ± 0.09	12.27	17.29	29.89	1.14
(Bulge test) 100 mm diameter	29.61 ± 0.10

3.2.1 Effect of Bending and Temperature on Forming Limit Diagram. The corrected FLD was shown as dotted line after neglecting the bending strain in Fig. 8 at both room and elevated temperature of 200 °C. It can be observed that the corrected FLD shifted to a marginally lower position when compared to the experimentally measured FLD. Simultaneously, it shifted toward the tension-compression region by approximately 3.41 and 3.1% at room temperature and 200 °C, respectively. This shift was due to the induced bending strain from the 50-mm-diameter hemispherical punch during LDH testing, which was subtracted from the measured strain. As the true bending strain (ϵ_b) is not a constant value, rather a function of t_f and ρ , hence the repositioning of corrected FLD in downward direction was not uniform. However, the shift was lower at elevated temperature due to higher dome height of the specimens.

Significant improvements in the limiting strains were observed in the entire FLD at elevated temperature of 200 °C compared to that at room temperature. The FLD at 200 °C can be observed to shift in upward direction significantly as shown in Fig. 8(b), and the FLD_0 changed from 0.18 to 0.44 indicating 145% improvement. This enhancement in formability may be due to the drastic improvement in post-uniform elongation of the material delaying the onset of strain localisation at elevated temperatures. The equi-biaxial, plane strain, and tension-compression strain path of 20-mm-width Hasek (Ref 33) specimens are shown in FLDs. It can be observed that insufficient availability of data points in pure biaxial deformation at elevated temperature due to experimental limitations enforced to do minute extrapolation to plot complete FLD.

3.3 Limiting Dome Height Validation

Table 6 summarizes the comparison of experimental LDH with predicted values for all specimen geometries used in the experiment. The dome heights were predicted by FE simulation implementing the Cowper-Symonds constitutive equations with and without incorporating the strain rate sensitive parameters (C and p values). It was found that closer dome height as that of experimental result was predicted at 200 °C when incorporating the strain rate sensitive parameters in FE modeling, however, the results were under predicted otherwise. These LDH results give insight into the influence of strain rate sensitive parameters to be crucial in helping the increase in formability at elevated temperature. However, the LDH results were predicted close to the experimental results without incorporating the C and p parameters at room temperature. The error in prediction lies reasonably within 0.14 to 3.27%, in an acceptable range. These minor variations may be attributed to the assumption of a constant friction coefficient. Also, the several rate-dependent properties like thermal conductivity, convective, and radiation heat transfer coefficient were assumed in FE simulations, and a small error will significantly influence the simulation results due to adoption of the time-scaling method.

As the material possesses very encouraging ductility the fracture in all specimens was not sudden, rather after the occurrence of visible localized necking. In all FE simulation, the necking location was predicted very close to that observed in the experiments. The comparative representation of experimental and predicted LDH at elevated temperature for biaxial

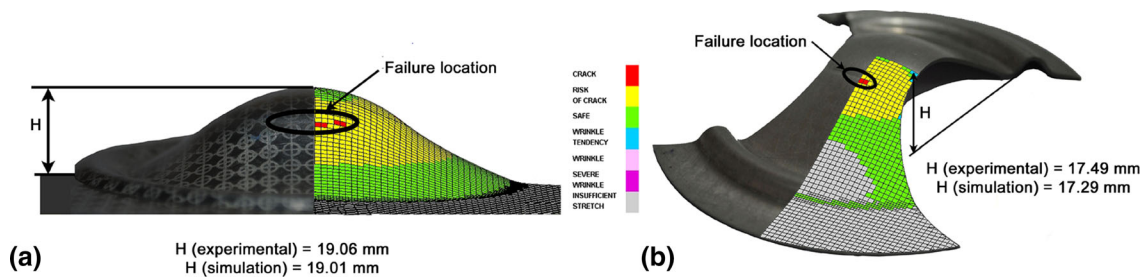


Fig. 10 Experimental and FE predicted LDH comparison after stretch formed at elevated temperature at 200 °C: (a) biaxial specimen and (b) Hasek specimen

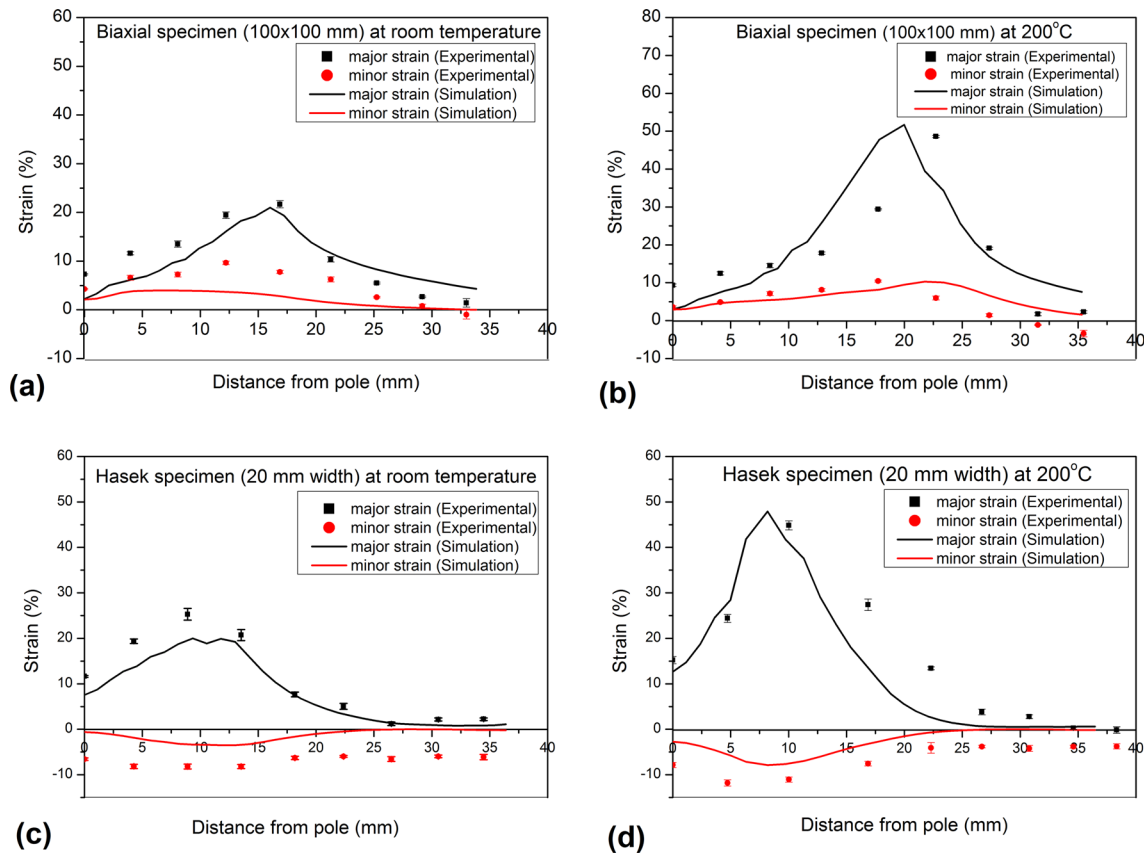


Fig. 11 Strain distribution profile of biaxial specimen deformed at (a) room temperature and (b) 200 °C; and Hasek specimen deformed at (c) room temperature and (d) 200 °C

and Hasek specimens with failure location is depicted Fig. 10. It can be found that the failure location from the pole in the stretch formed components shifted depending on the geometry of the specimen, e.g., 11 mm in case of Hasek specimen and 20 mm in case of biaxial specimens, both deformed at elevated temperature. This may be due to the strain distribution developed in the component depending on the geometry and strain path during deformation.

3.3.1 Strain Distribution Profile. The major and minor strains were measured on surface of the biaxial and Hasek specimens, and these data were plotted with respect to the distance from the pole to represent the strain distribution profile. The comparison of strain distribution profile of the deformed cups at room temperature and 200 °C is shown in

Fig. 11. The FE predicted results were also incorporated to validate the results. It can be observed that both the major and minor strains are positive values indicating biaxial tensile deformation mode for 100 × 100 mm specimens during LDH testing both at room temperature and 200 °C (Fig. 11a, b). The strains were observed to be very well developed in the specimens when deformed at elevated temperature due to the higher LDH. The location of peak strains was observed to shift away from the pole with rise in temperature due to the redistribution of strain depending on the material flow on surface of the heated punch. In case of the Hasek specimens, the minor strain was negative indicating the tension-compression deformation mode due to the lateral drawing of the material during LDH test, as shown in Fig. 11(c) and (d).

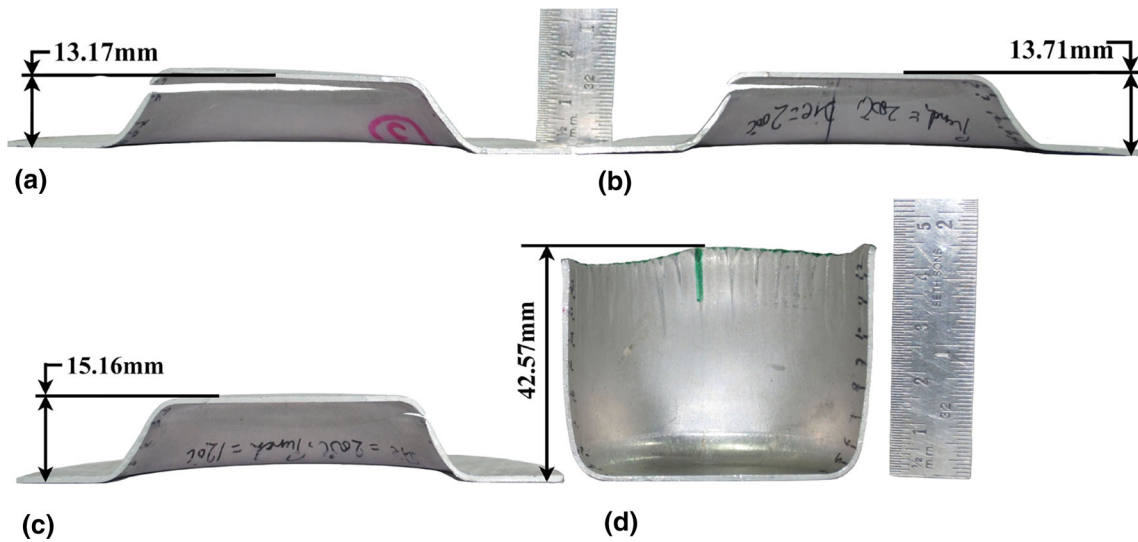


Fig. 12 Deep drawn cups obtained from initial blank diameter of 110 mm at different die and punch temperature combinations: (a) 30 and 30 °C; (b) 200 and 200 °C; (c) 200 and 120 °C; and (d) 200 and 30 °C

Similar to biaxial tensile deformation, the peak strain increased significantly at elevated temperature during tension-compression deformation mode. However, the location of peak strain did not change due to the specimen geometry with lesser material at the center of the Hasek specimen. Hence, the failure was observed consistently closer to the pole compared to that in biaxial specimen. The FE-predicted strain distribution trend can be observed to be in good agreement with measured values.

3.4 Deep Drawing Behavior

Deep drawing experiments were performed using 110-mm circular blanks under four different tooling temperature conditions as described in section 2.2.3. The deep drawn cups obtained from these four different isothermal and non-isothermal conditions are shown in Fig. 12 with the cup depth indicating the influence of tool temperature. In all the elevated temperature deep drawing experiments, the die was kept consistently at 200 °C and the punch temperature was varied to three different temperatures, i.e., 200, 120 °C, and room temperature. The cup depth increased marginally from 13.17 mm at room temperature to 13.71 mm when both the punch and die were heated to 200 °C. Further, the cup depth was increased to 15.16 mm when the punch temperature was reduced to 120 °C, and this indicated the influence of non-isothermal condition. However, the circular blank was drawn completely with an average cup depth of 42.57 mm when the punch temperature was further brought down to room temperature by water circulation.

The comparison of thickness distributions measured from the bottom center to the top edge of the cup is shown in Fig. 13. The close view of the thinning development in all the experimentally drawn cup is also shown. In all the drawn cups, the maximum thinning took place at the cup bottom corner. However, it can be observed that the thinning development reduces in non-isothermal deep drawing process. Hence, a bigger cup could be drawn by providing temperature gradient within the blank in warm forming. Also, significant thickening of 35% in the upper wall was observed in a completely drawn cup due to the circumferential/hoop com-

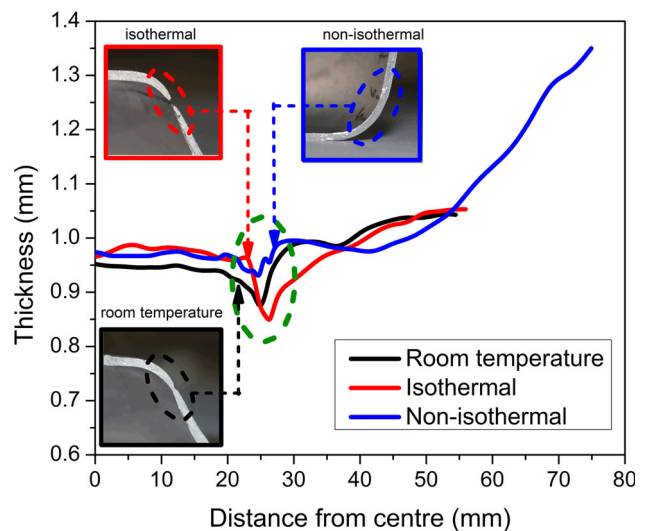


Fig. 13 Thickness distribution in experimental deep drawn cups for different die and punch temperature combinations with close view of thinning development

pressive stress. It was also found that too much temperature difference between the die and punch temperature resulted in early failure at cup top corner because of higher temperature flange material.

3.5 FE Validation of Deep Drawing Process

The cup height predicted from the thermo-mechanical FE simulation was compared with the experimental results for all the four different isothermal and non-isothermal deep drawing cases. It can be seen in Fig. 14 that predicted cup heights are in better agreement with experimental results within a reasonable error of 5%. The thickness distribution with maximum thinning development was predicted very close to the experimental results, as shown in Fig. 15. The minor change in thickness was observed on the flat bottom portion of the cup due to the

negligible deformation because of the frictional force between the sheet and punch interface from the start of the deep drawing process. On further punch movement, the flange materials were

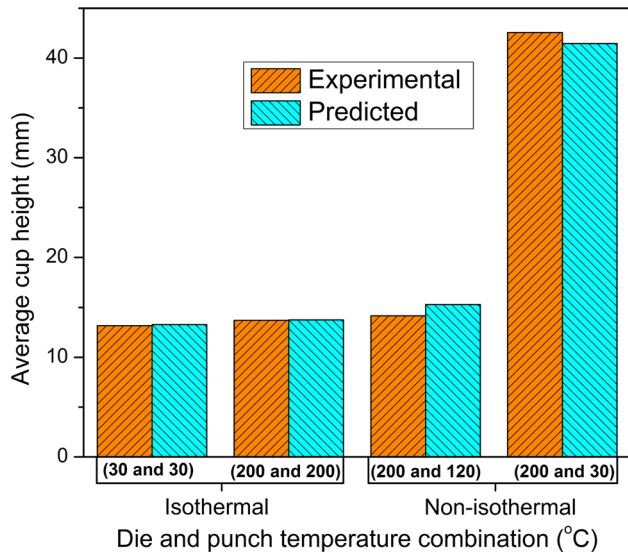


Fig. 14 FE validation of deep drawn cup heights for different die and punch temperature combinations

drawn into the die cavity and the material flow was not uniform due to the difference in resistance offered by the material in different direction because of the anisotropic properties. This mechanism of material flow led to wavy top edge, often referred as earing, in a completely drawn cup as observed in non-isothermal deep drawing process. To determine the earing profile, cup height was measured at different locations of cup with an increment of 6° angular position from rolling direction. The earing profile and % earing (i.e., $((H - h)/h) \times 100$, where H was cup height at any location and h was the minimum height) predicted by FE simulation was validated with experimental earing profile. It can be observed that the FE simulation was able to capture the earing defect in reasonable agreement with experimental values (Fig. 16a, b). Total four ears having peak heights at 0° , 90° , 180° , and 270° with respect to the rolling direction were observed in the present study due to the positive planar anisotropy (i.e., $\Delta R = \frac{1}{2}(R_0 - 2R_{45} + R_{90}) > 0$).

3.5.1 Insight into Formability Improvement in Non-isothermal Deep Drawing. To get insight into the formability improvement, finding the temperature distribution in the cup during deformation is very important. The flow properties of the material were already found to be influenced heavily on the temperature during deformation. Further, to validate the FE model, the blank center temperature (BCT) was measured during the progress of deep drawing experiment, as this portion within the blank was easily accessible for inserting the thermocouple. Fig. 17 shows the comparison of FE predicted

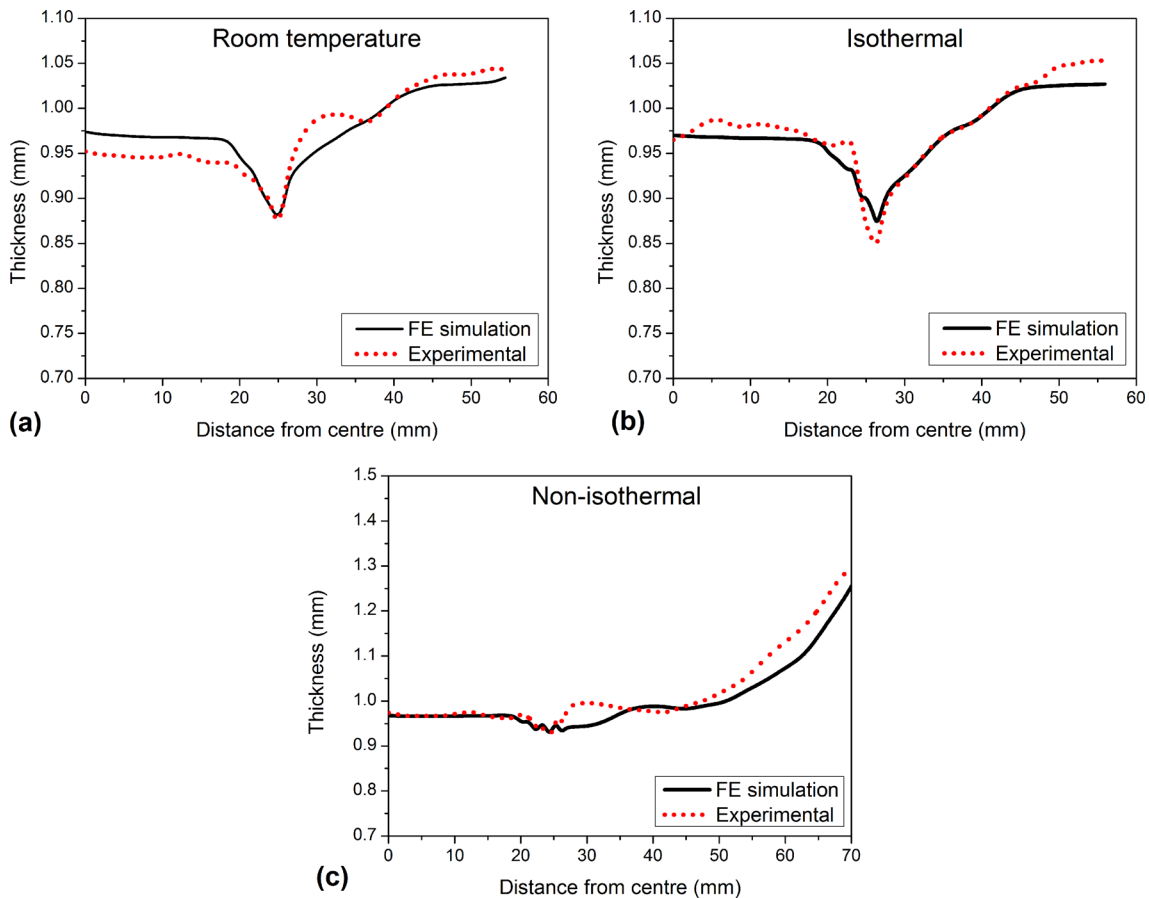


Fig. 15 FE validation of thickness distribution in deep drawn cups: (a) room temperature; (b) isothermal (200 °C); and (c) non-isothermal (punch at room temperature and die at 200 °C)

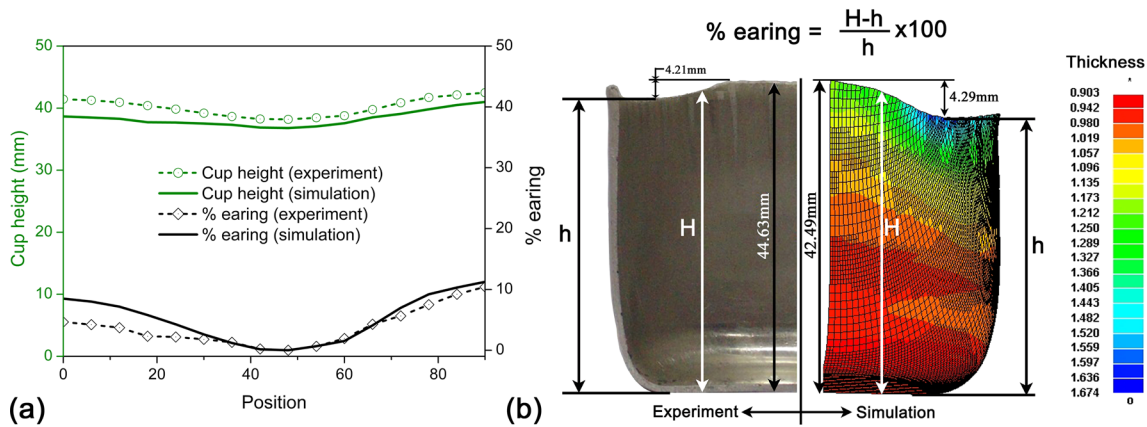


Fig. 16 (a) FE validation of earing profile and pct. earing and (b) comparative demonstration of earing profile in non-isothermal deep drawn cups

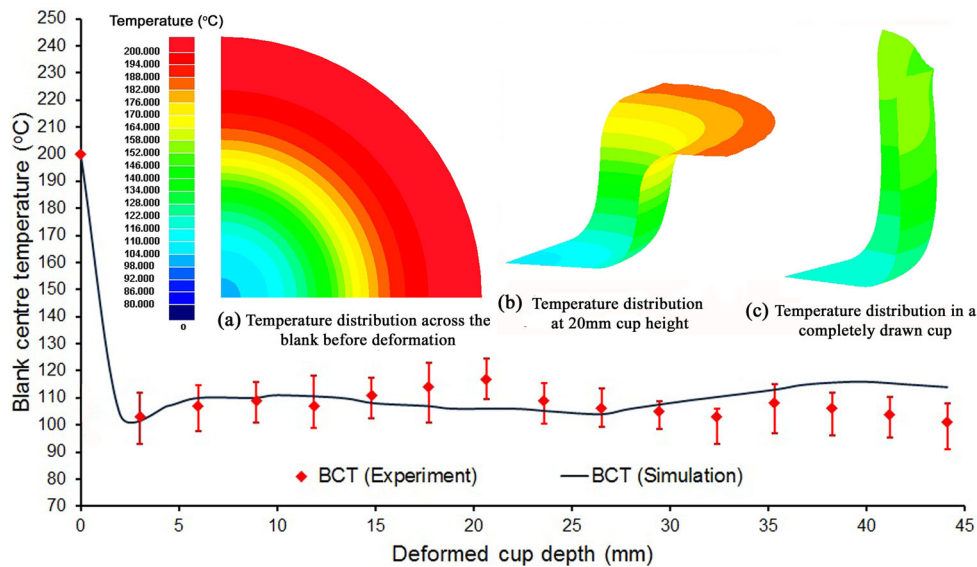


Fig. 17 Validation of blank center temperature (BCT) with temperature distribution across the blank at different deformation steps

and experimental measured BCT with progression of cup height. As per the adopted process sequence in section 2.2.1, the blank got heated up uniformly to 200 °C after placing between heated die and binder. The temperature at bottom portion of the blank decrease instantly to 107 °C once it came in contact with the water-circulated cooler punch (Fig. 17a), and this established approximately 93 °C temperature difference across the blank. This is due to the conductive heat transfer from the blank to punch before the start of deformation. In order to establish a steady BCT, the punch was allowed to be in touch with the blank for about 5 s. It can be observed in Fig. 17 that BCT remain almost constant throughout the deformation process and similar result is predicted by FE simulation as well. In the flange region two different conduction heat transfer processes took place, and these are (i) from flange to blank center due to significant temperature difference between them and (ii) from both die and binder to flange due to contact. As the punch progressed down, the first phenomenon dominate over second, therefore the flange temperature

decreased as shown in Fig. 17a-c. The transient temperature distribution profile developed within the blank during deformation process can be observed at different time steps. Hence, the different regions within the cup were maintained at different temperature during the deep drawing process, and this helped in controlling the material flow into the die cavity. The punch corner and flange region temperature was captured from FE simulation at an intermediate cup depth (Fig. 18a), and it was found that the flange region and the cup corner were at 180 and 140 °C, respectively. The flow properties of the AA5754-H22 alloy were already observed to be significantly influenced by the temperature, and the strength was found to decrease with the increase in temperature. The Barlat-89 yield locus incorporating the temperature-dependent properties was plotted at room temperature, 140 and 200 °C to represent the change in biaxial stress state of the material with respect to different temperature condition (Fig. 18b). It can be seen that the yield locus is bigger for 140 °C and it shrinks drastically at 200 °C. Hence, the strength of the material at the cup bottom corner

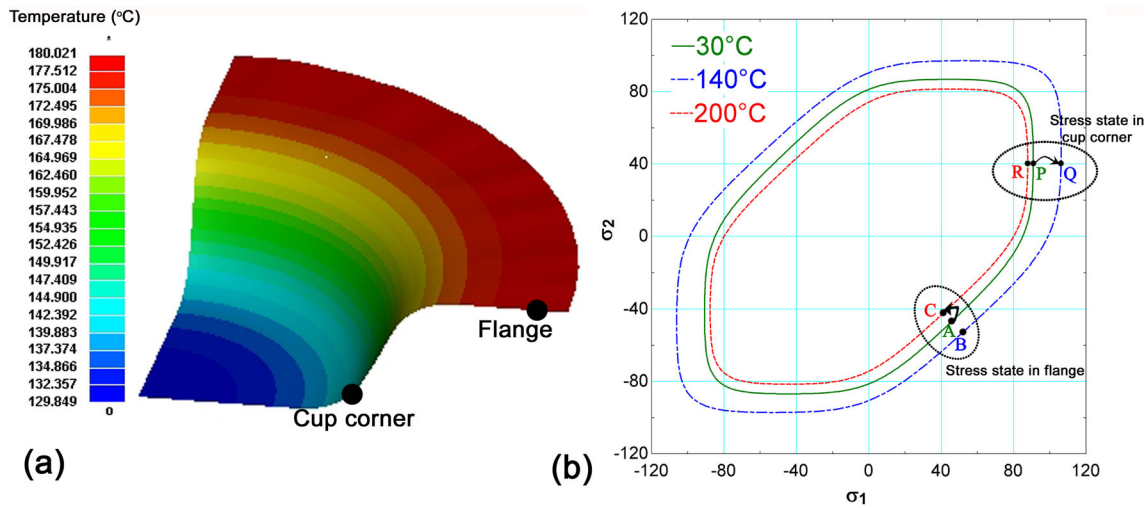


Fig. 18 (a) Deformed cup at an intermediate step representing the temperature variation and (b) Influence of temperature on Barlat-89 yield locus for AA5754-H22

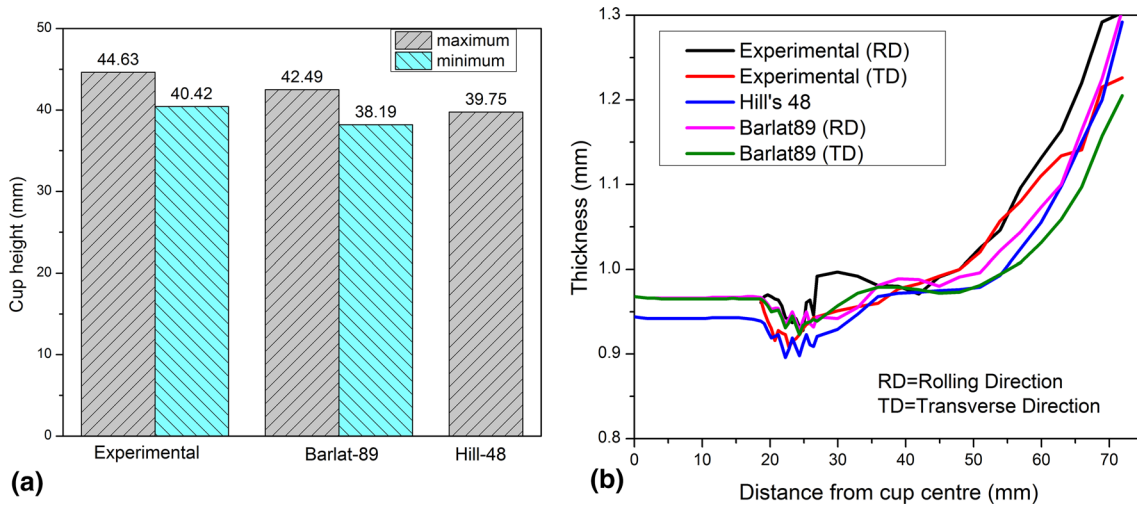


Fig. 19 Influence of yield criteria in FE predictions: (a) cup height and (b) thickness distribution

maintained at 140 °C increased to state Q with simultaneous decrease in strength of flange material to state C. This helped in easy material flow from the flange with simultaneous increase in the strength of the cup wall in order to draw a bigger cup successfully.

3.6 Influence of Planar Anisotropy

Thermo-mechanical FE simulation was also carried out using the Hill-48 yield criterion incorporating only normal anisotropy parameter. The cup height obtained from this yield criterion neglecting the planar anisotropy could not able to predict the wavy ear profile, and hence it was concluded that the earing defect was due to the planar anisotropy in the material during non-isothermal deep drawing. The maximum and the minimum cup height obtained from the deep drawing experiments are compared with FE predicted results using both the Barlat-89 and Hill-48 yield criterion as shown in Fig. 19(a), and it can be observed that the Barlat-89 yield criterion is

predicting better results than Hill-48 yield criterion. It can be observed in Fig. 19(b) that different thickness distributions with thinning development along both the rolling and transverse directions were predicted very well by the Barlat-89 yield criterion. However, the Hill-48 model could not able to predict this difference in thickness distribution in different section as it neglected the planar anisotropy.

3.7 Effect of Deformation Mode on Thinning Development

The susceptibility of further deformation can be identified from the evolution of thinning in a formed component. Hence, the pattern of thinning development was compared due to the influence of different forming modes used in the present studies, namely stretch forming and deep drawing process. The true thickness strain variation along normalized distance from the cup center (or pole) is shown in Fig. 20. The normalized distance is used to negate the effect of punch diameter, but the effect of deformation mode on thickness distribution can be

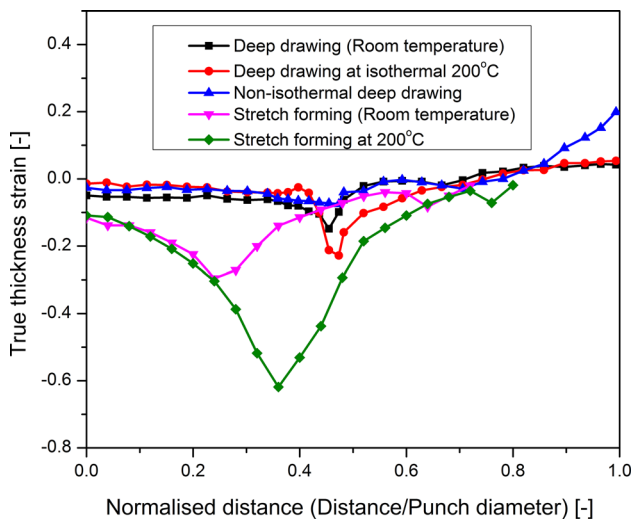


Fig. 20 Effect of deformation mode on thinning development in different warm forming processes

observed. In the hemispherical stretch forming, the material exposed above the die cavity gets stretched through biaxial tensile stress which led to thinning of material. Hence the thickness strain was negative, and the maximum thinning took place corresponding to the location of peak surface major strain. The maximum thinning location during stretch forming was found to shift away from the pole with increase in deformation temperature. In deep drawing process, the deformation of the blank took place due to the radial tensile and circumferential compressive deformation mode, and further the blank bends and unbends across the die corner radius while flowing into the die cavity. The complete load during deep drawing process was supported by the cup wall and hence thinning was observed consistently at the punch corner due to strain localization. Further, the thickness distribution and thinning development during deep drawing was different compared to the stretch forming process as observed in Fig. 20. Positive thickness strain indicating thickening of the cup wall was noticed at the top of the deep drawn cup due to the circumferential compressive stress.

4. Conclusions

The deep drawing and stretch forming test setup were developed to carry out laboratory scale isothermal and non-isothermal formability testing, and the following are the major conclusions made from the experimental and FE studies:

- (a) The uniaxial tensile test results showed that the AA5754-H22 alloy was temperature and strain rate dependent. The total elongation increases from 24.5% at room temperature to 86.5% at elevated temperature of 250 °C, and the PLC effect reduced significantly both at elevated temperature and higher strain rate. The Cowper-Symonds constitutive equation was established successfully by incorporating the temperature-dependent hardening parameters (K and n value) and strain rate sensitive parameters C and p .

- (b) The limiting strains were evaluated by carrying out the LDH test of different specimen geometries both at room temperature and elevated temperature (200 °C). The effect of punch curvature and temperature on the FLD was established. There was very negligible influence of bending strain developed due to the hemispherical punch used in the present LDH tests. However, the FLD shifted upward drastically at 200 °C with 145% improvement in the FLD_0 .
- (c) The thermo-mechanical FE model was developed successfully coupling the Barlat-89 yield criterion with the established Cowper-Symonds constitutive equations incorporating temperature-dependent anisotropy parameters. The LDH was predicted within 5% error compared to the experimental results. The FE simulation results suggested that the improvement in LDH at elevated temperature was due to the strain rate sensitivity of the AA5754-H22 material, which improved the surface strain distribution and delayed the onset of necking.
- (d) The influence of tooling temperature was investigated by conducting deep drawing experiments at different die and punch temperature combinations to understand the control of material flow due to temperature gradient. The significant improvements in cup heights were observed when the die was heated to 200 °C and the punch was maintained at room temperature. The FE simulation of this deep drawing condition predicted that a non-isothermal temperature distribution was established in the blank with a maximum temperature difference of 93 °C from flange to center.
- (e) The improvement in formability in non-isothermal deep drawing process was due to the increase in the strength of the cup wall maintained at lower temperature and simultaneous easier flow of flange material held above the die at higher temperature. This helped in reduction in thinning development at the cup bottom corner, and hence the 110-mm-diameter blank was deep drawn successfully. The Barlat-89 anisotropy material model could able to predict the earing profile and thickness distributions in different direction with respect to rolling direction due to accurate incorporation of temperature dependent planar anisotropy properties. It was also concluded that the thickness distribution and the thinning location depended on the deformation mode inherited from the tool geometry and the forming process.

Acknowledgment

Authors are thankful to Mr. Chandan Mondal, Metal Forming Laboratory, Department of Mechanical Engineering, IIT Kharagpur for his help while conducting sheet metal forming experiments.

References

1. S. Toros, F. Ozturk, and I. Kacar, Review of Warm Forming of Aluminum-Magnesium Alloys, *J. Mater. Process. Technol.*, 2008, **207**, p 1-12
2. V. Psyk, D. Risch, B.L. Kinsey, A.E. Tekkaya, and M. Kleiner, Electromagnetic Forming—A Review, *J. Mater. Process. Technol.*, 2011, **211**, p 787-829

3. S.H. Zhang, Z.R. Wang, Y. Xu, Z.T. Wang, and L.X. Zhou, Recent Developments in Sheet Hydroforming Technology, *J. Mater. Process. Technol.*, 2004, **151**, p 237-241
4. D.V. Wilson, Aluminium Versus Steel in the Family Car—The Formability Factor, *J. Mech. Work. Technol.*, 1988, **16**, p 257-277
5. S. Mahabunphachai, M. Koc, and J.E. Carsley, Investigations on Deformation Behavior of AA5754 Sheet Alloy Under Warm Hydroforming Conditions, *J. Manuf. Sci. Eng.*, 2011, **133**, p 051007
6. J. Jeswiet, M. Geiger, U. Engel, M. Kleiner, M. Schikorra, J. Dufflou, R. Neugebauer, P. Bariani, and S. Bruschi, Metal Forming Progress Since 2000, *CIRP J. Manuf. Sci. Technol.*, 2008, **1**(2008), p 2-17
7. R.C. Picu, G. Vincze, F. Ozturk, J.J. Gracio, F. Barlat, and A.M. Maniatty, Strain Rate Sensitivity of the Commercial Aluminum Alloy AA5182-O, *Mater. Sci. Eng. A*, 2005, **390**, p 334-343
8. P.J. Bolt, R.J. Werkhoven, A.H. Van Den Boogaard, Warm Deep Drawing of Aluminium Sheet, 2003, p 2-9
9. F. Ozturk, S. Toros, and H. Pekel, Evaluation of Tensile Behaviour of 5754 Aluminium-Magnesium Alloy at Cold and Warm Temperatures, *Mater. Sci. Technol.*, 2009, **25**, p 919-924
10. D. Li and A. Ghosh, Tensile Deformation Behavior of Aluminum Alloys at Warm Forming Temperatures, *Mater. Sci. Eng. A*, 2003, **352**, p 279-286
11. M. Jain, J. Allin, and M.J. Bull, Deep Drawing Characteristics of Automotive Aluminum Alloys, *Mater. Sci. Eng. A*, 1998, **256**, p 69-82
12. S. Yoshihara, K.I. Manabe, and H. Nishimura, Effect of Blank Holder Force Control in Deep-Drawing Process of Magnesium Alloy Sheet, *J. Mater. Process. Technol.*, 2005, **170**, p 579-585
13. G. Palumbo and L. Tricarico, Numerical and Experimental Investigations on the Warm Deep Drawing Process of Circular Aluminum Alloy Specimens, *J. Mater. Process. Technol.*, 2007, **184**, p 115-123
14. H.S. Kim, M. Koç, J. Ni, and A. Ghosh, Finite Element Modeling and Analysis of Warm Forming of Aluminum Alloys—Validation Through Comparisons with Experiments and Determination of a Failure Criterion, *J. Manuf. Sci. Eng.*, 2006, **128**, p 613
15. D.E. Green, K.W. Neale, S.R. MacEwen, A. Makinde, and R. Perrin, Experimental Investigation of the Biaxial Behaviour of an Aluminum Sheet, *Int. J. Plast.*, 2004, **20**, p 1677-1706
16. D. Li and A.K. Ghosh, Biaxial Warm Forming Behavior of Aluminum Sheet Alloys, *J. Mater. Process. Technol.*, 2004, **145**, p 281-293
17. T. Naka, G. Torikai, R. Hino, and F. Yoshida, The Effects of Temperature and Forming Speed on The Forming Limit Diagram for Type 5083 Aluminum-Magnesium Alloy Sheet, *J. Mater. Process. Technol.*, 2001, **113**, p 648-653
18. F. Barlat and K. Lian, Plastic Behavior and Stretchability of Sheet Metals. Part I: A Yield Function for Orthotropic Sheets Under Plane Stress Conditions, *Int. J. Plast.*, 1989, **5**, p 51-66
19. J.W. Yoon, F. Barlat, R.E. Dick, K. Chung, and T.J. Kang, Plane Stress Yield Function for Aluminum Alloy Sheets. Part II: FE Formulation and Its Implementation, *Int. J. Plast.*, 2004, **20**, p 495-522
20. M. Zampaloni, N. Abedrabbo, and F. Pourboghrat, Experimental and Numerical Study of Stamp Hydroforming of Sheet Metals, *Int. J. Mech. Sci.*, 2003, **45**, p 1815-1848
21. T. Naka, Y. Nakayama, T. Uemori, R. Hino, and F. Yoshida, Effects of Temperature on Yield Locus for 5083 Aluminum Alloy Sheet, *J. Mater. Process. Technol.*, 2003, **140**, p 494-499
22. D.G. Tari and M.J. Worswick, Elevated Temperature Constitutive Behavior and Simulation of Warm Forming of AZ31B, *J. Mater. Process. Technol.*, 2015, **221**, p 40-55
23. ASTM, E8/E8M Standard Test Methods for Tension Testing of Metallic Materials, *Annu. B. ASTM Stand.*, 2010, **4**(2010), p 1-27
24. S.K. Panda, D.R. Kumar, H. Kumar, and A.K. Nath, Characterization of Tensile Properties of Tailor Welded IF Steel Sheets and Their Formability in Stretch Forming, *J. Mater. Process. Technol.*, 2007, **183**, p 321-332
25. Livermore Software Technology Corporation, LS-DYNA Keyword User's Manual, Version 971, California (2007)
26. R. Courant, Variational Methods for the Solution of Problems of Equilibrium and Vibrations, *Bull. Am. Math. Soc.*, 1943, **49**, p 1-23
27. T. Belytschko, J.I. Lin, and T. Chen-Shyh, Explicit Algorithms for the Nonlinear Dynamics of Shells, *Comput. Methods Appl. Mech. Eng.*, 1984, **42**, p 225-251
28. H. Karbasian and A.E. Tekkaya, A Review on Hot Stamping, *J. Mater. Process. Technol.*, 2010, **210**, p 2103-2118
29. R. Hill, A Theory of the Yielding and Plastic Flow of Anisotropic Metals, *Proc. R. Soc. London A Math. Phys. Eng. Sci.*, 1948, **193**, p 281-297
30. J. Winkhofer, G. Trattnig, C. Lind, C. Sommitsch, H. Feuerhuber, F. Barlat, Y.H. Moon, M.G. Lee, Process Simulation of Aluminium Sheet Metal Deep Drawing at Elevated Temperatures, 2010, p 927-934
31. N. Abedrabbo, F. Pourboghrat, and J. Carsley, Forming of Aluminum Alloys at Elevated Temperatures - Part 2: Numerical Modeling and Experimental Verification, *Int. J. Plast.*, 2006, **22**, p 342-373
32. P.L. Charpentier, Influence of Punch Curvature on the Stretching Limits of Sheet Steel, *Metall. Trans. A*, 1975, **6**, p 1665-1669
33. V. Hasek, Research and Theoretical Description Concerning the Influence on the FLDs, *Blech Rohre Profile*, 1978, **25**, p 213-220